



The Return of the Rosetta Target: Keck Near-infrared Observations of Comet 67P/Churyumov–Gerasimenko in 2021

Boncho P. Bonev¹, Neil Dello Russo², Hideyo Kawakita³, Ronald J. Vervack Jr.², Michael A. DiSanti⁴, Yoshiharu Shinnaka³, Takafumi Ootsubo^{5,6}, Erika L. Gibb⁷, Michael R. Combi⁸, Kathrin Altwegg⁹, Nicolas Biver¹⁰, Jacques Crovisier¹⁰, Gregory Doppmann¹¹, Geronimo L. Villanueva⁴, Younas Khan⁷, Chemed T. Ejeta⁷, Mohammad Saki¹², Adam J. McKay¹³, Anita L. Cochran¹⁴, Emmanuel Jehin¹⁵, Nathan X. Roth^{16,17}, Martin A. Cordiner^{16,17}, and Yinsi Shou⁸

¹ Department of Physics, American University, 4400 Massachusetts Avenue, NW, Washington, DC 20016, USA; bonev@american.edu

² Space Department, Johns Hopkins University Applied Physics Laboratory, Laurel, MD 20723, USA

³ Koyama Astronomical Observatory, Kyoto Sangyo University, Motoyama, Kita-ku, Kyoto 603-8555, Japan

⁴ Solar System Exploration Division, Planetary Systems Laboratory, MS 693, NASA Goddard Space Flight Center, Greenbelt, MD 20771, USA

⁵ National Astronomical Observatory of Japan, 2-21-1 Osawa, Mitaka, Tokyo 181-8588, Japan

⁶ University of Occupational and Environmental Health Japan, Kitakyushu 807-8555, Japan

⁷ Department of Physics and Astronomy, University of Missouri-St. Louis, Saint Louis, MO 63121, USA

⁸ Department of Climate and Space Sciences and Engineering, University of Michigan, Ann Arbor, MI 48109, USA

⁹ Physikalisches Institut, Universität Bern, Sidlerstr. 5, CH-3012 Bern, Switzerland

¹⁰ LESIA, Observatoire de Paris, Université PSL, CNRS, Sorbonne Université, Université de Paris, 5 place Jules Janssen, F-92195 Meudon, France

¹¹ W. M. Keck Observatory, Kamuela, HI 96743, USA

¹² Physics Department, Auburn University, Auburn, AL 36832, USA

¹³ Department of Physics and Astronomy, Appalachian State University, Boone, NC 28608-2106, USA

¹⁴ McDonald Observatory, University of Texas at Austin, Austin, TX 78712, USA

¹⁵ STAR Institute—University of Liège, Allée du 6 Août 19C, B-4000 Liège 1, Belgium

¹⁶ Department of Physics, Catholic University of America, Washington, DC 20064, USA

¹⁷ Solar System Exploration Division, Astrochemistry Laboratory Code 691, NASA Goddard Space Flight Center, 8800 Greenbelt Road, Greenbelt, MD 20771, USA

Received 2023 May 3; revised 2023 July 27; accepted 2023 August 4; published 2023 November 10

Abstract

High-resolution near-infrared ground-based spectroscopic observations of comet 67P/Churyumov–Gerasimenko near its maximum activity in 2021 were conducted from the W. M. Keck Observatory, using the facility spectrograph NIRSPEC. 67P is the best-studied comet to date because of the unprecedented detail and insights provided by the Rosetta mission during 2014–2016. Because 67P is the only comet where the detailed abundances of many coma volatiles were measured in situ, determining its composition from the ground provides a unique opportunity to interpret Rosetta results within the context of the large database of ground-based compositional measurements of comets. However, previous apparitions, including in 2015, have been unfavorable for in-depth ground-based studies of parent volatiles in 67P. The 2021 apparition of 67P was thus the first-ever opportunity for such observations. We report gas spatial distributions, rotational temperatures, production rates, and relative abundances (or stringent upper limits) among seven volatile species: C₂H₂, C₂H₆, HCN, NH₃, CH₃OH, H₂CO, and H₂O. The measured abundances of trace species relative to water reveal near average or below average values compared to previous comets studied at infrared wavelengths. Both gas rotational temperatures and the spatial distributions of H₂O, C₂H₆, and HCN measured with Keck-NIRSPEC in 2021 are consistent with the outgassing patterns revealed by Rosetta in 2015 at very similar heliocentric distance (post-perihelion). These results can be integrated with both Rosetta mission findings and ground-based cometary studies of the overall comet population, for which we encourage a wide-scale collaboration across measurement techniques.

Unified Astronomy Thesaurus concepts: Solar system (1528); Small Solar System bodies (1469); Comets (280); Short period comets (1452); Comae (271); Neutral coma gases (2158)

1. Introduction

This work reports high-resolution ($\lambda/\Delta\lambda \sim 25,000$) near-infrared (near-IR) ground-based spectroscopic observations of comet 67P/Churyumov–Gerasimenko (hereafter 67P/C-G), conducted during its uncommonly favorable apparition in 2021. Comets are small volatile-rich bodies formed early in the history of the solar system. Compositional measurements of cometary volatiles are an essential link to understanding planetary system formation because comets retain ices from

the dense cold regions of the protosolar disk midplane. The midplane is the central region in the vertical structure of a protoplanetary disk (PPD), where ices freeze on dust grains, and where cometary nuclei eventually form (Willacy et al. 2015; Kamp 2020). However, the densest parts of the midplanes of extra-solar PPDs are largely opaque to observations, making measurements of the volatile inventory of comets an important (and accessible) window to the midplane chemistry of a forming PPD (Eistrup et al. 2019; Willacy et al. 2022). Furthermore, the icy cometary nuclei are leftover material from the formation of planets. Gravitational scattering triggered by the young giant planets eventually redistributed many nuclei toward their dynamical reservoirs: the Oort cloud and the scattered Kuiper disk (Gladman 2005). Today, various

processes can gravitationally perturb individual comets from these reservoirs back to the inner solar system. Most newly discovered comets come from the Oort cloud, while the scattered Kuiper disk is the main source of ecliptic comets, including Jupiter-family comets (JFCs; Levison 1996). As a comet approaches the Sun, sublimation leads to the development of a coma (exosphere). Coma gases can either originate directly from nucleus ices (referred to as native or parent volatiles, for example C_2H_2 , H_2O , CH_3OH , etc.) or be produced in the coma via photodissociation or other processes (product species; for example, CN, C_2 , OH, H, etc.).

The link between comets and planetary system formation has been the main motivation for extensive studies of these objects via both remote sensing and spacecraft missions (Bauer et al. 2023; Biver et al. 2023a; Knight et al. 2023; Snodgrass et al. 2023). The target of our observations, comet 67P/C-G, is a short-period (6.4 yr) JFC that has a special significance because it was explored in unprecedented detail by the ESA Rosetta mission (2014–2016). An important legacy of Rosetta is the complexity of information on the composition of parent volatiles released into the coma of 67P/C-G, as sensed by multiple instruments (Le Roy et al. 2015; Bockelée-Morvan et al. 2016; Biver et al. 2019; Rubin et al. 2019; Lauter et al. 2020). These include the largest suite of volatiles ever measured in a comet—from noble gases, through water and simple prebiotic compounds (C_2H_6 , NH_3 , etc.), to the amino acid glycine and many other complex organics (Altwegg 2022). Abundances of isotopologues (Altwegg et al. 2017; Muller et al. 2022) and of heteroatoms relative to carbon (Hanni et al. 2022) suggest that the ices of 67P/C-G contain strong heritage from the protosolar cloud. Interpretations of mission data continue.

Because missions are restricted to only a few visited targets, astronomical remote sensing is essential for enabling enough observations to understand comets as a population (Biver et al. 2023a). Product species have been studied extensively during multiple apparitions of 67P/C-G (Cochran et al. 1992, 2012; A’Hearn et al. 1995; Crovisier et al. 2002; Feldman et al. 2004; Schulz et al. 2004; Schleicher 2006; Fink 2009; Lara et al. 2011; Bertaux et al. 2014; Guilbert-Lepoutre et al. 2014; Snodgrass et al. 2016, 2017; Knight et al. 2017; Ivanova et al. 2017; Opitom et al. 2017; Bair et al. 2022; Vander Donckt et al. 2023; and references therein). A comprehensive overview of gas production rates of several product species, as measured at optical and UV wavelengths, is given by Ivanova et al. (2017). In contrast, radio and IR ground-based observations of parent molecules require higher sensitivities. Such observations were therefore almost nonexistent before 2021 for 67P/C-G due to unfavorable apparitions with large geocentric distances ($\Delta > 1.6$ au). Remote sensing measurements of parent volatiles in 67P/C-G in 2015 included only several upper limits, along with detections of HCN and CH_3OH using millimeter-wave spectroscopy (Snodgrass et al. 2017; Biver et al. 2023b). The return of the Rosetta target in 2021 was thus highly anticipated because of its exceptionally favorable observing geometry ($\Delta \approx 0.4$ au). This apparition provided the first-ever opportunity for in-depth ground-based investigations of its parent volatiles, urgently needed for the most accurate comparison with mission results. The measurements reported here are the missing link, tying the unique Rosetta findings for 67P/C-G to the compositions determined for many comets using established (and uniformly implemented) ground-based techniques.

Here we present IR measurements with the NIRSPEC spectrograph on the Keck II telescope (Martin et al. 2018). A significant aspect of these observations is measuring abundances of symmetric hydrocarbons C_2H_2 and C_2H_6 , which can be sensed only in the IR. Symmetric hydrocarbons are measured simultaneously with the most abundant coma gas (H_2O) and trace species HCN, NH_3 , CH_3OH , and H_2CO . This same suite of volatiles has been studied in a number of comets, thereby providing a basis for comparison. CH_3OH , H_2CO , and HCN were also measured by coordinated millimeter/submillimeter studies (Biver et al. 2023b), thereby linking the two techniques. We report gas spatial distributions, rotational temperatures, production rates, and relative abundances among species. These results can be integrated with both mission and ground-based cometary studies, for which we encourage a wide-scale collaboration across measurement techniques.

2. Keck II Observations of 67P/Churyumov–Gerasimenko

During apparitions before Rosetta, ground-based observations provided evidence that the outgassing of 67P/C-G is dominated by seasonal effects (Schleicher 2006; Bertaux et al. 2014). Rosetta indeed revealed extreme seasonal changes, with a short but intense southern summer near the 2015 perihelion, when the sunlit part of the nucleus lost a few meters from its surface (Hansen et al. 2016; Combi et al. 2020). The perihelion distance (q) of 67P/C-G decreased by $\sim 2.6\%$ in 2021 (1.21 au, on UT November 2) compared to 2015 (1.24 au). Sharma et al. (2021) and Kelley et al. (2021) reported a significant outburst on 2021 November 17 and estimated an order of magnitude larger mass loss than the typical outburst seen by Rosetta. Our first observing date was on November 28, at heliocentric distance $R_h = 1.26$ au (see Table 1) and was near the period of maximum brightness, as suggested by the visual light curve.¹⁸ Assuming seasonal changes followed the pattern revealed in 2015, the 2021 November 28 Keck measurements were contemporaneous with peak outgassing (about three weeks after perihelion), and close to the southern summer solstice. Our subsequent observations occurred approximately three weeks later, on 2021 December 16 ($R_h = 1.33$ au).

Table 1 shows a condensed observing log. We utilized two NIRSPEC settings per night, both including strong lines of H_2O together with trace parent volatiles. The KL1 setting (echelle/cross-disperser angle = $64^\circ.11/32^\circ.83$) encompasses the brightest emissions of C_2H_6 (ethane), simultaneously with CH_3OH (methanol). The KL2 setting ($62^\circ.18/32^\circ.92$) samples a weaker band of C_2H_6 , but is optimized for HCN (hydrogen cyanide), C_2H_2 (acetylene), NH_3 (ammonia), and H_2CO (formaldehyde). On December 16 a mechanical shift in echelle grating position caused the last group of KL2 frames to be processed separately; hence there are two entries in Table 1 for KL2 on that date.

Long-slit spectra were obtained using a standard A–B–B–A sequence of telescope nodding, with both the A and B beams in the slit, symmetrically displaced to either side of slit center and separated by $12''$ (half the slit length). NIRSPEC simultaneously can take spectra in L -band while the slit-viewing camera images in the K band. Using offset nonsidereal guiding relative to a nearby field star, we applied fine adjustments to the comet position based on these K -band images, ensuring it remained at the proper A-beam or B-beam position. The

¹⁸ <http://www.aerith.net/comet/catalog/0067P/2021.html>

Table 1
Observing Log

UT Date (2021)	R_h^a (au)	Δ^a (au)	$d\Delta/dt^{a,b}$ km s ⁻¹	T_{int}^c (min.)	Slit PA	Sun–Comet PA	Phase angle	NIRSPEC Setting ^d
28 Nov	1.255	0.424	1.0	47	337°	280°	43°	KL1
28 Nov	1.255	0.424	1.1	77	337°	280°	43°	KL2
16 Dec	1.330	0.444	2.5	61	277°	277°	32°	KL1
16 Dec	1.331	0.445	2.8	153 ^e	277°	277°	32°	KL2
16 Dec	1.332	0.445	3.1	10	277°	277°	32°	KL2

Notes.

^a R_h , Δ , and $d\Delta/dt$ are, respectively, heliocentric distance, geocentric distance, and topocentric line-of-sight velocity of 67P/C-G.

^b At near-zero Doppler shift, lines of cometary methane (CH₄) covered by the spectral range of the NIRSPEC settings were obscured by their counterpart absorptions in the Earth’s atmosphere.

^c Here, T_{int} is the total integration time on source, after accounting for reading out the NIRSPEC array.

^d The KL2 setting generally requires longer integration times because it samples species with comparatively weaker IR lines (C₂H₂ and NH₃).

^e This data set was used to derive the rotational temperatures, production rates, and relative abundances listed in Table 2 for UT December 16. All three sets for KL2 listed in this table were used to combine spectra from both observing dates, as discussed in Section 3.1.

methodology for data acquisition, reduction, and spectral analysis is detailed elsewhere and was validated against recent comet observations with NIRSPEC (Boney et al. 2021).

3. Results

3.1. Spectral Fits

The multi-panel Figure 1 shows extracted spectra. A slit width of 0".432 enabled a resolving power of $\lambda/\Delta\lambda \approx 25,000$. Spectra look similar on both dates, so representative examples are shown. The measured spectrum is displayed at the top of each panel. A best-fit model (pink) of the near-IR dust continuum accounts for the wavelength-dependent telluric extinction and is overlaid against the measured spectrum. The atmospheric transmittance function was tightly constrained from both comet and contemporaneous standard star data using the Planetary Spectrum Generator¹⁹ (Villanueva et al. 2018).

Molecular emissions can be seen in excess of the continuum. Molecular emission models are color coded and shown below each measured spectrum to help identify IR lines—those of H₂O (Figures 1(a) and (b)) and C₂H₆ (1c) are the easiest to discern. Models of other species are scaled vertically (e.g., HCN $\times 2$; 1d) to better show the expected line positions. Each model accounts for terrestrial atmospheric transmittance and is based on previously tested emission efficiencies (g-factors (photons s⁻¹ mol⁻¹); Villanueva et al. 2011b, 2022, and references therein).

Secure detection of a molecule requires identifying at least several of its IR lines in the spectrum. This criterion is met for H₂O, C₂H₆ (ν_7 band; Figure 1(c)), and HCN. Because these lines are optically thin, comparing modeled and measured spectra allows for determining gas spatial distributions and rotational temperatures (Section 3.2), production rates (Section 3.3), and relative abundances (Section 3.4). Stochastic (related to photon noise) and systematic uncertainties are evaluated in these parameters following Dello Russo et al. (2004), Boney (2005), and Villanueva et al. (2011a).

When no individual lines are detected, the signal-to-noise ratio (S/N) can be improved by summing the signal over several expected line positions, as described by Villanueva et al. (2009), possibly leading to a tentative detection. Section 3.4 discusses the specific cases for C₂H₂ and CH₃OH in the context of measured abundances. An additional increase

in S/N is achieved by coadding spectra from the two observing dates (Figure 1(e)). However, for tentatively detected and non-detected species (for example, NH₃ in Figure 1(d)) the integration times (Table 1) were sufficient to constrain their abundances to significant limits on each observing date. This eliminated additional uncertainties specific to coadding spectra taken 2.5 weeks apart (for example, applying vastly different telluric corrections from November 28 and December 16).

3.2. Gas and Dust Spatial Distributions and Gas Rotational Temperatures

Figure 2 shows the long-slit spatial profiles of the near-IR dust continuum, and of volatiles with brighter emissions. The profiles of C₂H₆ and HCN are noisier than that of H₂O, so they were smoothed by 3. Distributions are asymmetric with respect to the peak of the comeasured continuum profile. On November 28, the gas and dust profiles are more extended toward the position angle (PA) of the south pole for 67P/C-G, as derived from Rosetta observations at equivalent R_h and season. The slit orientation was changed on December 16 to be aligned with the projected Sun–comet direction on the sky, revealing sunward-extended profiles. The distributions on both dates are consistent with a fan-shaped coma, approximately oriented toward the Sun, as observed by Rosetta (Biver et al. 2019; Cheng et al. 2022). This suggests similar outgassing patterns in 2015 and 2021 during equivalent R_h (post-perihelion) and season, when outgassing occurred mainly from regions in the comet’s southern hemisphere, while preferentially exposed to the Sun (Läuter et al. 2022).

The relative intensities of emission lines depend on the gas rotational temperature (T_{rot}), defined as the Boltzmann temperature that best approximates the rotational population distribution within the ground vibrational state of a molecule. Boney et al. (2014) describe the T_{rot} retrieval methods, which combine standard excitation analysis (Dello Russo et al. 2004) with global fits using T_{rot} as a parameter (Figure 1). Retrieved T_{rot} (Table 2) generally agree among species, as predicted by thermodynamic models for the collisional inner coma (Bodewits et al. 2023).

Table 2 shows T_{rot} for a nucleus-centered extract, where spectral line intensities are highest. The best S/N H₂O spectra in the KL2 NIRSPEC setting (from December 16, when integration time was the longest) also allowed for obtaining temperatures at three off-nucleus positions along the slit (Figure 2(d)). The footprint area for each measurement

¹⁹ <https://psg.gsfc.nasa.gov/>

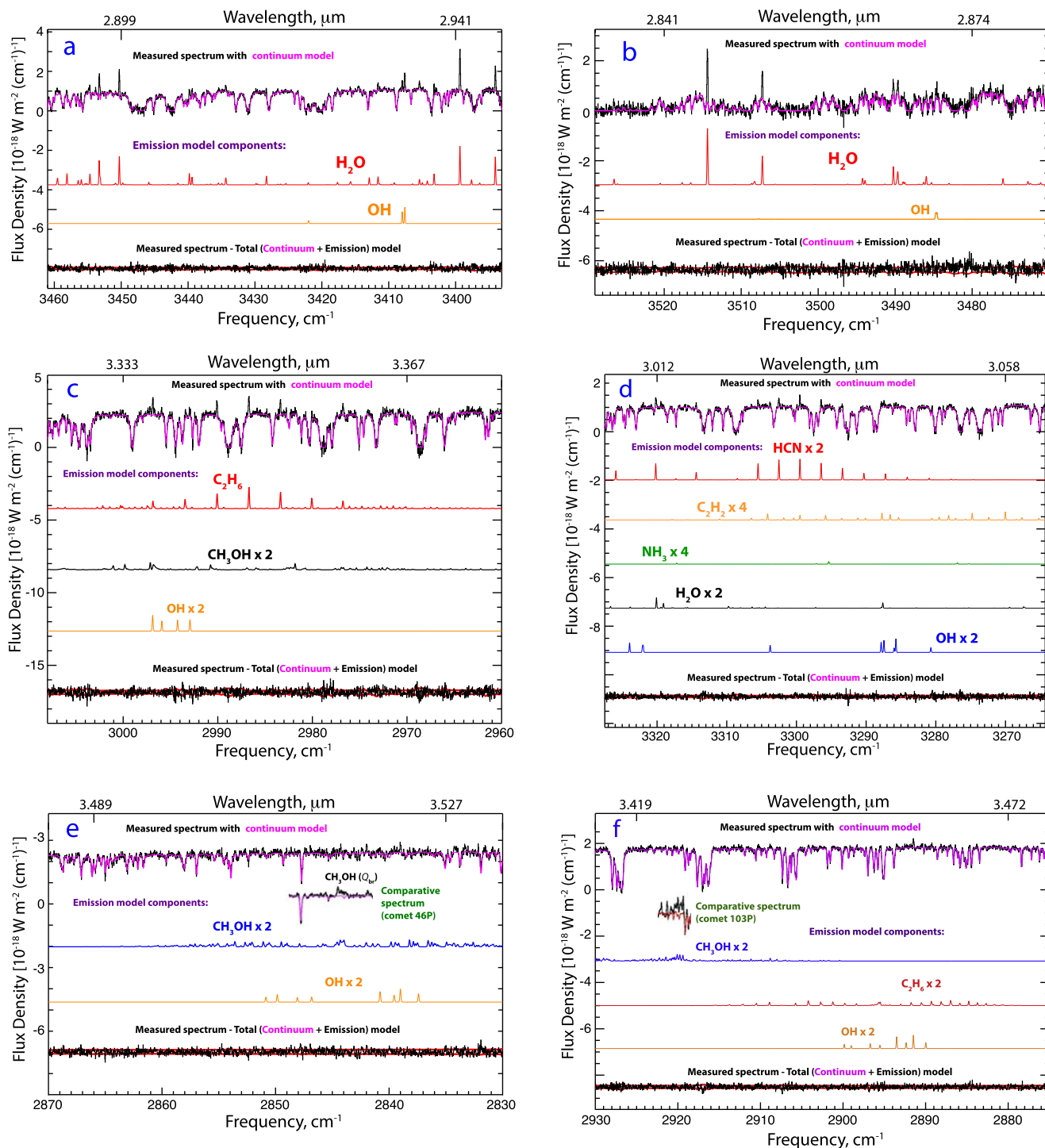


Figure 1. Spectra of comet 67P/Churyumov–Gerasimenko, covering various wavelength ranges. Each spectrum consists of two components: a near-IR continuum, and molecular emissions in excess of the continuum. In each figure panel, a best-fit continuum model (in pink) is overlaid against the measured spectrum. Molecular emission models are color coded and shown below the measured spectrum. The photon noise ($\pm 1\sigma$) envelope is indicated by red lines in the “Measured spectrum—Total model” plot (bottom of each figure panel). (a)–(b) Emission of H_2O from UT November 28 (panel (a)) and December 16 (b), illustrating bright IR lines in the KL2 and KL1 NIRSPEC settings, respectively. (c) Spectrum of C_2H_6 (UT November 28; KL1). All spectral peaks in the C_2H_6 emission model (red) belong to the ν_7 vibrational band of this species. (d) Detection of HCN on UT December 16 (KL2). The integration time (Table 1) was sufficient to tightly constrain the NH_3 and C_2H_2 abundances, even at the absence of secure detection. ((e)–(f)) The main wavelength ranges to search for CH_3OH in the KL1 (panel (e)), coadded spectra from both observing dates) and KL2 (panel (f), UT December 16) settings. Comparative spectra from other comets are shown as inserts to contrast with the low gas-to-continuum ratio in 67P/C-G, where individual lines of CH_3OH could be discerned above the strong continuum only at much higher abundance (see Section 3.4.3). The ν_3 band of C_2H_6 (emission model in red in panel (f)), is significantly weaker than the ν_7 band (panel (c)).

corresponds to 139 km (slit width) times the distance range along the slit marked with horizontal bar through each measurement point (375 km, except for the most distant point,

where we integrated the signal over a larger range, 708 km, to achieve sufficient S/N). A decrease in T_{rot} can be traced along the slit in the sunward direction, consistent with near-adiabatic

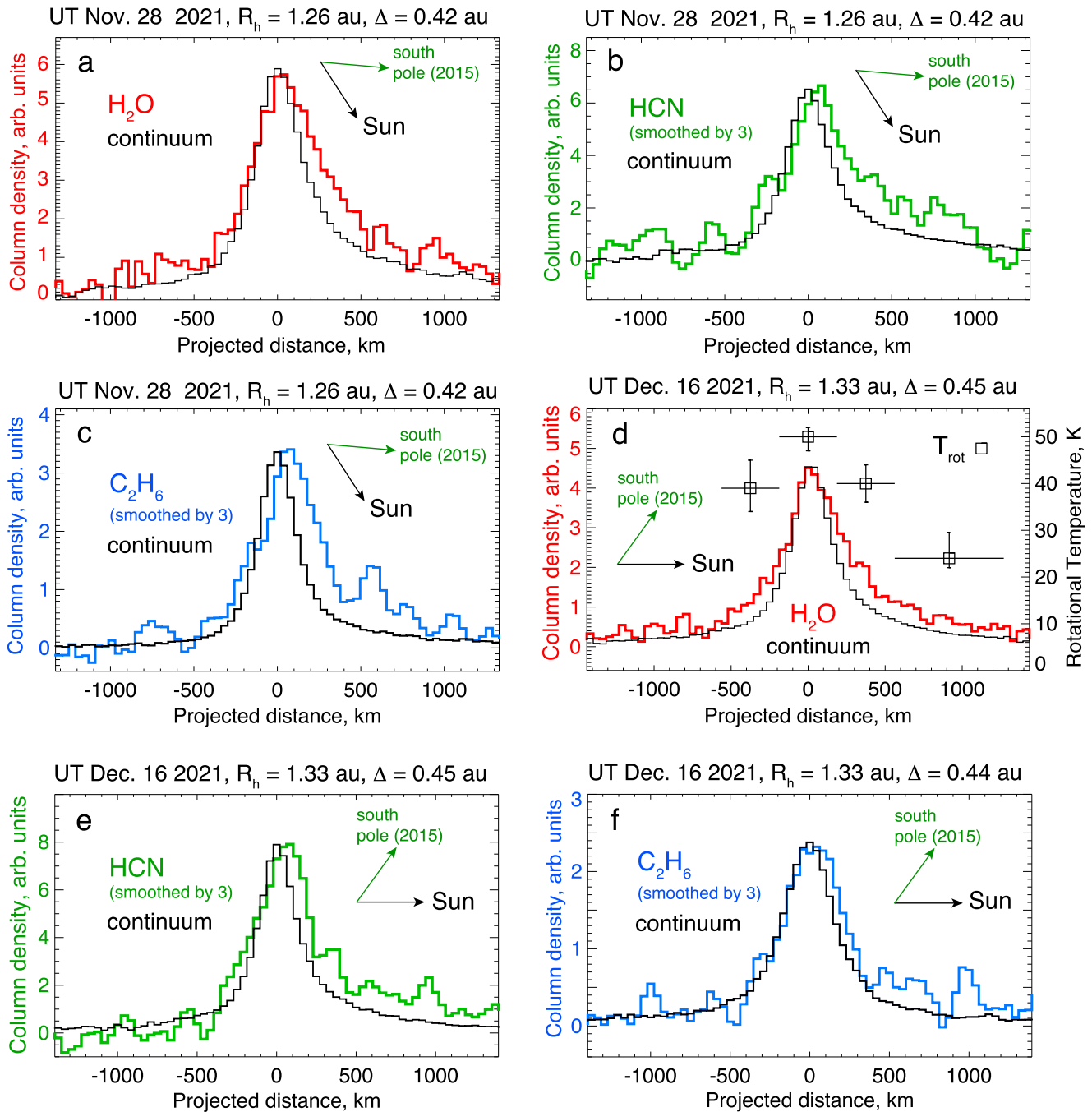


Figure 2. Spatial distributions for H₂O, HCN, C₂H₆, and dust (comeasured with each species) with observing date indicated on each plot. Panel (d), also shows measurements of H₂O gas rotational temperature, as discussed in Section 3.2.

expansion cooling (Fougere et al. 2012). The S/N for spectra taken in the antisunward direction at distances $> \sim 600$ km is insufficient for a robust T_{rot} retrieval, although the spectral fits suggest $T_{rot} < 30$ K. Overall, the measured T_{rot} are quite similar to in situ retrievals for the corresponding post-perihelion R_h (2015 September) from the Microwave Instrument for the Rosetta Orbiter (MIRO) submillimeter telescope (Biver et al. 2019; Table A2). Contemporaneous (to our Keck study) T_{rot} measurements by the Institut de Radioastronomie Millimétrique (IRAM) telescope (~ 36 K; Biver et al. 2023b) are also in agreement with Rosetta data but are lower than T_{rot} for our nucleus-centered extracts (~ 50 K), as expected given the larger field-of-view (FoV) of IRAM (~ 3000 km).

3.3. Gas Production Rates: Uncertainties and Comparison with Previous Apparitions

Table 2 shows nucleus-centered production rates (Q_{nc}) and global production rates (Q) derived by the well documented Q -curve method (Xie & Mumma 1996; DiSanti et al. 2001, 2016; Villanueva et al. 2011a). This formalism provides the ratio Q/Q_{nc} , referred to as the “growth factor” (GF). It accounts for slit losses in flux due to atmospheric seeing, hence, $GF > 1$. In addition, differences in GF for comeasured (i.e., affected identically by seeing) species may reflect differences in their spatial profiles. For example, although the H₂O and HCN distributions (Figures 2(d) and (e)) show similar sunward asymmetry, the water profile is overall more extended, resulting in a larger GF.

Table 2
Molecular Production Rates and Relative Abundances in 67P/C-G

UT Date (2021)	Setting	Mol	T_{rot}^a [K]	Q_{nc}^b [10^{25} s^{-1}]	GF ^b	Q^b [10^{25} s^{-1}]	Relative Abundance ^c	
Nov. 28	KL1	H ₂ O	48 ± 6	855 ± 27	2.41 ± 0.10	2061 ± 107	100	
		C ₂ H ₆	42 ⁺⁸ ₋₆	2.01 ± 0.08	2.19 ± 0.39	4.40 ± 0.80	0.21 ± 0.04	
		CH ₃ OH	(48)	4.92 ± 0.87	(2.41)	11.9 ± 2.2	0.58 ± 0.10	
	KL2	H ₂ O	52 ± 3	715 ± 30	2.39 ± 0.11	1710 ± 106	100	
		HCN	48 ⁺⁷ ₋₆	0.90 ± 0.05	2.57 ± 0.34	2.32 ± 0.33	0.14 ± 0.02	
		NH ₃	(48)	<3.92	(2.39)	<9.36	<0.55	
		C ₂ H ₂	(48)	<0.393	(2.39)	<0.939	<0.055	
		C ₂ H ₆	(50)	2.57 ± 0.27	2.17 ± 0.41 ^e	5.58 ± 1.20	0.33 ± 0.07	
		H ₂ CO	(50)	<0.576	(2.39)	<1.38	<0.081	
Dec. 16	KL1	H ₂ O	43 ± 4	603 ± 17	2.62 ± 0.09	1579 ± 71	100	
		C ₂ H ₆	(43)	1.88 ± 0.19	1.74 ± 0.10	3.26 ± 0.38	0.21 ± 0.03	
		CH ₃ OH	(43)	5.20 ± 0.85	(2.62)	13.6 ± 2.3	0.86 ± 0.14	
	KL2	H ₂ O	50 ± 3	606 ± 24	2.29 ± 0.07	1387 ± 69	100	
		HCN	45 ⁺⁵ ₋₄	0.94 ± 0.06	1.70 ± 0.10	1.60 ± 0.14	0.12 ± 0.01	
		NH ₃	(45)	<1.62	(2.29)	<3.70	<0.27	
		C ₂ H ₂	(45)	0.305 ± 0.059	(2.29)	0.699 ± 0.137	0.050 ± 0.010	
		C ₂ H ₆	(50)	1.81 ± 0.29	1.52 ± 0.11 ^e	2.75 ± 0.48	0.20 ± 0.04	
		H ₂ CO	(50)	<0.317	(2.29)	<0.727	<0.052	
		CH ₃ OH ^d		3.95 ± 0.70	(2.29)	9.04 ± 1.62	0.65 ± 0.12	

Notes.

^a Gas rotational temperature for nucleus-centered aperture of 0.43" (slit width) x 1.16" (along slit). T_{rot} measured for different species are in good agreement on each observing date. Minor differences in T_{rot} do not significantly affect measured abundances. Values in parenthesis are assumed.

^b Nucleus-centered production rate (Q_{nc}), growth factor (GF), and global production rate ($Q = \text{GF} \times Q_{nc}$). Values of GF in parenthesis are assumed and discussed in Section 3.3.

^c Relative abundances are expressed as ratios of global production rates.

^d Based on empirical model for CH₃OH emission near 2920 cm⁻¹ (3.425 μm), which is currently under development. The resulting relative abundance agrees within uncertainty with that obtained from the KL1 setting.

^e Calculated under the assumption that the ratio of growth factors for H₂O and C₂H₆ in the KL2 setting, where only GF(H₂O) could be measured, is the same as the ratio in KL1.

Table 2 reports GF for H₂O, HCN, and C₂H₆. An often overlooked source of uncertainty is assuming a GF for species, for which spatial analysis is not feasible. For such species we justify the assumptions for their GF. We adopt the same GF for H₂O and CH₃OH, assuming that the outgassing of these volatiles near perihelion is sourced in similar regions of the nucleus (Biver et al. 2019; Läuter et al. 2022). We assume the same ratio between the growth factors of C₂H₆ and H₂O in the KL1 setting (where both are measured) applies to the KL2 setting (where a GF could be measured only for H₂O), thereby allowing us to calculate the GF for C₂H₆ in KL2. For the non-detected species NH₃ and H₂CO, we apply the GF for H₂O because it is equal to (within uncertainty) or is solely the largest measured GF in the setting. This assumption provides the most conservative (i.e., highest) upper limits.

Production rates also depend on rotational temperature, which is well constrained, as discussed in Section 3.2. However, Q is especially sensitive to the assumed gas outflow speed (v_{gas}). We adopted $v_{\text{gas}} = 0.8 \text{ (km s}^{-1}\text{)} \times R_h^{-0.5}$, consistent with mean expansion speeds measured in 67P/C-G by IRAM in 2021 (Biver et al. 2023b), and with v_{gas} near the 2015 perihelion obtained by fitting coma expansion models to gas distributions and local densities measured by Rosetta (Hansen et al. 2016; Combi et al. 2020). Assuming different v_{gas} would change proportionally the absolute Q , but has a negligible effect on relative abundances.

The water production rates, $Q(\text{H}_2\text{O})$, measured on each date from the KL1 and KL2 settings are in good agreement. Near the peak of the comet's activity we find $Q(\text{H}_2\text{O}) \approx 1.9 \times 10^{28} \text{ s}^{-1}$

(mean between KL1 and KL2; 2021 November 28). Eleven days earlier the Odin Sub-millimeter Observatory measured $Q(\text{H}_2\text{O}) = 1.2 \times 10^{28} \text{ s}^{-1}$ (Biver et al. 2023b). On 2021 December 16 $Q(\text{H}_2\text{O}) \approx 1.5 \times 10^{28} \text{ s}^{-1}$ based the Keck measurements. Five days earlier, observations of OH with the Hubble Space Telescope resulted in significantly lower production: $Q(\text{H}_2\text{O}) \approx 0.3 \times 10^{28} \text{ s}^{-1}$ (Noonan et al. 2023).

In 2015, atomic hydrogen Ly α observations by the Proximate Object Close Flyby with Optical Navigation (*PROCYON*) spacecraft reported $Q(\text{H}_2\text{O}) = 1.2\text{--}1.5 \times 10^{28} \text{ s}^{-1}$ (Shinnaka et al. 2017) at $R_h = 1.3 \text{ au}$ (post-perihelion). Photometric measurements of OH at Lowell Observatory led to $Q(\text{H}_2\text{O}) = 0.77 \times 10^{28} \text{ s}^{-1}$ at nearly the same R_h (Snodgrass et al. 2017). Shinnaka et al. (2017) reviewed remote sensing (ground-based and from space observatories) measurements from five apparitions between 1982 and 2015. These show a range of $Q(\text{H}_2\text{O})$ from ~ 0.6 to $\sim 2 \times 10^{28} \text{ s}^{-1}$ for post-perihelion R_h similar to those of our observations. Bertaux et al. (2014) obtained time series of $Q(\text{H}_2\text{O})$ from Solar and Heliospheric Observatory/Solar Wind Anisotropies instrument (SOHO/SWAN), based on hydrogen Ly α emission. These authors reported that apparition-to-apparition differences in $Q(\text{H}_2\text{O})$, measured shortly after perihelion (1.30, 1.70, and $0.57 \times 10^{28} \text{ s}^{-1}$, for 1996, 2002, and 2009 respectively) did not follow the corresponding changes in perihelion distance ($q = 1.30, 1.29, 1.25 \text{ au}$).

The maximum $Q(\text{H}_2\text{O})$ derived from Rosetta data is also sensitive to measurement technique. Based on MIRO, Biver et al. (2019) reported $0.8 \times 10^{28} \text{ s}^{-1}$. Based on Rosetta Orbiter Spectrometer for Ion and Neutral Analysis (ROSINA) data,

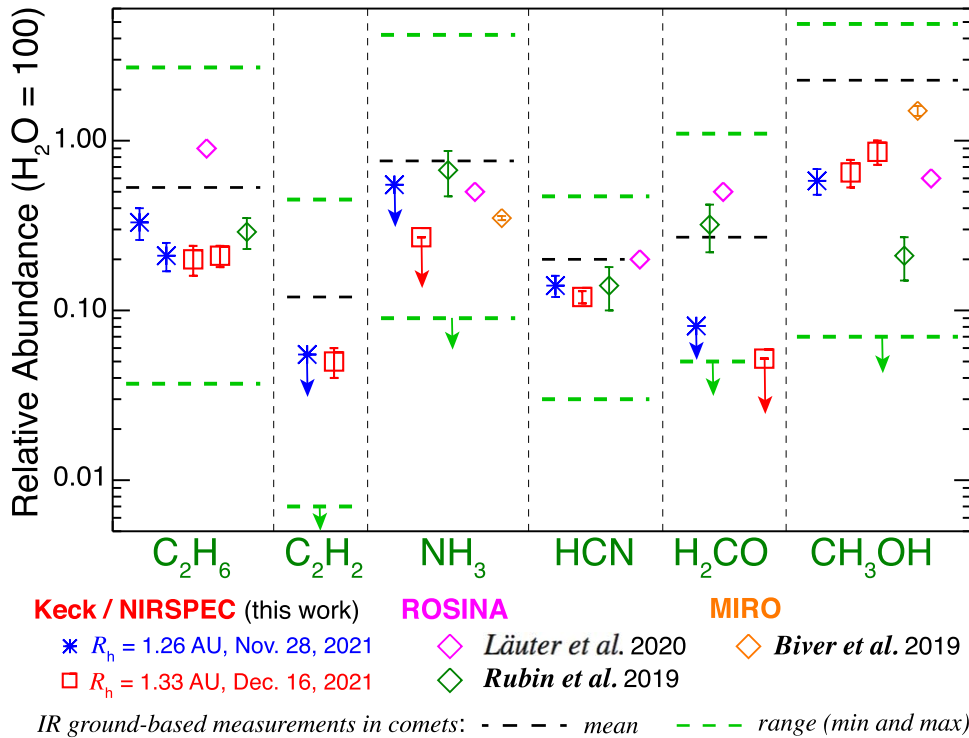


Figure 3. Relative abundances of volatiles measured in 67P/C-G by Keck in 2021. For comparison, the means and the ranges (minimum to maximum) of abundances obtained from infrared ground-based observations of other comets (Khan et al. 2023) are marked with black dashed and green dashed lines respectively. Downward errors indicate upper limits. Rosetta measurements are also shown. 67P/C-G is the best comet to date to discuss the similarities, differences, and uncertainties in results from various techniques (in situ and ground-based) applied to studies of volatiles. For this, we encourage a wide-scale collaboration across measurements techniques.

Läuter et al. (2020) calculated $Q(\text{H}_2\text{O})$ over successive time intervals. Their peak $Q(\text{H}_2\text{O})$ is $1.9 \times 10^{28} \text{ s}^{-1}$, corresponding to the interval between days 17 and 27 post-perihelion. Combi et al. (2020) reported production rates for successive 2 day intervals. Their peak values are: $Q(\text{H}_2\text{O}) \approx 0.5 \times 10^{28} \text{ s}^{-1}$ based on VIRTIS-H spectroscopic data, and $Q(\text{H}_2\text{O}) = 2.8 \times 10^{28} \text{ s}^{-1}$ based on ROSINA. We note that the ROSINA-based retrieval by Combi et al. (2020) is similar to that of Läuter et al. (2020), when the production rate is averaged over the same 11 day time interval.

In conclusion, the H_2O production rates from Keck are near the upper end of retrievals from both Rosetta measurements obtained during the period of maximum activity in 2015, and from remote sensing measurements from several apparitions. Because of the differences in $Q(\text{H}_2\text{O})$ from various techniques, it is not clear to what extent the $\sim 2.6\%$ decrease in perihelion distance between 2015 and 2021 has influenced the overall activity levels of 67P/C-G.

3.4. Relative Abundances of Targeted Volatiles

A highly anticipated outcome from the 2021 apparition of 67P/C-G has been a comparison between relative abundances ($\text{C}_2\text{H}_6/\text{H}_2\text{O}$, NH_3/HCN , etc.) from ground-based and in situ Rosetta studies. Abundances from Keck (Table 2) are expressed as ratios of global production rates of simultaneously measured species. For each given volatile, relative abundances from the two observing dates agree within uncertainty.

Figure 3 shows comparison with Rosetta measurements. Biver et al. (2019) reported relative abundances from MIRO, based on integrated mass loss over the entire mission. Rubin et al. (2019) deduced bulk nucleus abundances based on pre-perihelion ($R_h = 1.57$ to 1.51 au) ROSINA data. This period

was selected because Rosetta passed above the active (dayside) southern summer hemisphere, where enhanced outgassing provided fresh material from the comet’s interior. These authors also note the lack of outbursts driven by more volatile species during their selected time frame. Läuter et al. (2020) reported relative abundances (ROSINA) during peak activity, which were in good agreement with the ratios of time integrated production rates over the mission.

3.4.1. Symmetric Hydrocarbons: C_2H_6 and C_2H_2

Ethane is the most frequently detected trace species in IR cometary studies. Several IR lines of C_2H_6 (in the ν_7 band) are securely detected in the KL1 setting (Figure 1(c)). The weaker ν_5 band of C_2H_6 is sampled in the KL2 setting (Figure 1(f)). No individual ν_5 lines are detected at $\text{S/N} > 5$. However, summing the fluxes at multiple expected line positions leads to $\text{C}_2\text{H}_6/\text{H}_2\text{O}$ in agreement with the one obtained independently from KL1.

These results are similar to the bulk $\text{C}_2\text{H}_6/\text{H}_2\text{O}$ abundance deduced by Rubin et al. ($0.29\% \pm 0.06\%$) but are significantly lower than the abundance by Läuter et al. (0.9%).

We report a significant upper limit (November 28) and a marginal detection (December 16) of C_2H_2 . The latter is achieved by summing the flux over expected line positions, resulting in $Q(\text{C}_2\text{H}_2) \approx 5\sigma$ (Table 2; σ is the uncertainty). For the purposes of this study, the distinction between tentative detections and upper limits is secondary because, either way, the abundance is tightly constrained ($\text{C}_2\text{H}_2/\text{H}_2\text{O}$ is consistent with $\sim 0.05\%$). The $\text{C}_2\text{H}_2/\text{C}_2\text{H}_6$ ratio (~ 0.2) is similar to those measured by ROSINA at $R_h = 3.15$ au above the northern (summer) and southern (winter) hemispheres by Le Roy et al. (2015). The $\text{C}_2\text{H}_2/\text{H}_2\text{O}$ ratio agrees with the measurement by

Le Roy et al. (2015) above the summer hemisphere. Acetylene was also securely detected by ROSINA near perihelion (Hänni et al. 2022), allowing potentially for comparison at a similar R_h as our study.

The Keck abundance ratios C_2H_2/H_2O and C_2H_6/H_2O fall near the low end of measurements among comets. However, acetylene is especially underrepresented in compositional studies. The reported abundance provides one of the most stringent constraints to date in a JFC from the ground.

3.4.2. Nitrogen-bearing Species: HCN and NH_3

Hydrogen cyanide was securely detected with HCN/H_2O similar to the ROSINA retrieval by Rubin et al. (2019). The slightly larger value from Lauter et al. (2020) is due to the higher $Q(HCN)$ at peak activity in 2015 than the one measured with Keck in 2021. The abundances of NH_3 relative to H_2O from MIRO and ROSINA are intermediate between our two reported upper limits. The one from December 16 is more stringent, mainly due to the longer time on source. Our upper limits for NH_3/HCN (4.0 and 2.3 on November 28 and December 16, respectively) are intermediate between the ROSINA retrieval at peak outgassing (~ 2.7).

3.4.3. Oxidized-carbon Species: CH_3OH and H_2CO

Individual emission features of CH_3OH were not securely detected (Figure 1(e)), so the resulting abundance ($CH_3OH/H_2O \approx 0.6\%–0.9\%$) is based on coadding the signal at the expected line positions. This restriction stems from the combination of exceptionally strong continuum with weak gas emissions. These emissions could individually be discerned above the continuum only at much higher abundances of CH_3OH than those retrieved in 67P/C-G. To illustrate this, a comparative spectrum (comet 46P/Wirtanen) is shown, contrasting the low gas-to-continuum ratio in 67P/C-G with a typical secure CH_3OH detection, showing emissions prominently above the continuum.

The spectral region in Figure 1(e) is optimal to measure CH_3OH in comets through its ν_3 band lines. We also applied an empirical model (Feaga et al. 2022) of CH_3OH emission near 2920 cm^{-1} (Figure 1(f)). Although this model is still under development, the resulting abundance agrees within uncertainty with that from the ν_3 band, for which the g-factors are better validated (Table 2).

ROSINA and MIRO analyses led to different CH_3OH/H_2O values (Figure 3), owing mainly to the lower $Q(H_2O)$ retrieved by MIRO. The Keck measurements suggest $CH_3OH/H_2O < 1\%$, consistent with the ROSINA retrievals near peak activity.

Our reported upper limits of formaldehyde fall below the values from ROSINA retrievals and H_2CO/H_2O measured by remote sensing in most other comets (Dello Russo et al. 2016).

4. Discussion

Before 2021, the Rosetta findings were compared to detailed ground-based studies of parent volatiles in comets other than 67P/C-G. However, the IR observations presented here, as well as coordinated radio observations with IRAM (Biver et al. 2023b) allow for connecting in situ measurements for trace species (C_2H_2 , CH_3OH , etc.) with coma abundances from remote sensing of the same volatiles in the same comet. Thus, the uniform ground-based techniques applied to the analysis of

67P/C-G allow its composition to be put into context of the overall chemical taxonomy of the comet population. Despite observed differences (Figure 3), both Rosetta and ground-based abundances of C_2H_2 , HCN, NH_3 , CH_3OH , and H_2CO relative to water reveal near average or below average values compared to previous comets studied in the IR. The one exception is the significantly higher abundance of C_2H_6 as reported by Lauter et al. (2020). Assuming the seasonal pattern in 2015 was followed in 2021, comparing Keck results with these measurements is interesting because they correspond to the same time period (~ 3 weeks after perihelion). The difference with Keck is due to the higher $Q(C_2H_6)$ derived from ROSINA in 2015, while their $Q(H_2O)$ was almost identical to the one from our IR study.

The other significant difference is the extremely low abundance of H_2CO measured in 2021, contrasting the ROSINA-based results by both Lauter et al. (2020) and Rubin et al. (2019), which fall near the mean value of IR measurements in comets to date. The stringent upper limits from Keck are consistent with contemporaneous radio observations of 67P/C-G in 2021, assuming H_2CO is a parent volatile (Biver et al. 2023b). These authors emphasize H_2CO may instead be a fragment species with a Haser scale length of $\sim 8,000$ km, a scenario that explains our low abundance considering the much smaller FoV in the IR. This scenario is also supported by ALMA maps of H_2CO emission in several other comets, which strongly suggest that formaldehyde may be a fragment species, released predominantly from a progenitor source in the coma (Cordiner et al. 2023, and references therein). However, the precursor of H_2CO is presently unknown, particularly given that in 67P/C-G Hanni et al. (2022) find no evidence of polymerized formaldehyde in the ROSINA data.

An obvious challenge in comparing production rates and relative abundances is the non-contemporaneous nature of observations—in situ and ground-based studies of 67P/C-G are separated by a full orbital period. Despite the different apparitions, the spatial distributions of H_2O , C_2H_6 , and HCN measured by Keck in 2021 are consistent with the outgassing patterns revealed by Rosetta in 2015 during very similar R_h (post-perihelion) and season (southern summer). Measured rotational temperatures and their spatial distribution are also in good agreement with those obtained in situ during the mission, considering the observing geometry of the ground-based data. Together these findings suggest similar outgassing patterns during consecutive perihelion passages. Optical studies of products species and dust morphology, which unlike the IR cover the more extended coma, have brought several lines of evidence supporting fairly repeatable seasonal changes across apparitions. Analyzing observations from the 1982/83 and 1995/96 apparitions, Schleicher (2006) showed that the peak production rate occurred about a month after perihelion, consistent with the time series of gas production rates monitored by Rosetta. This work also showed significant sunward asymmetry in dust distribution, as observed (albeit on a much smaller spatial scale) in parent gas species (H_2O , C_2H_6 , and HCN) by Keck. Knight et al. (2017) reported that the pole orientation and active areas on 67P/C-G have been relatively stable over at least three apparitions before Rosetta, with changes in coma morphology primarily driven by the subsolar latitude.

An open question is whether or not the apparition-to-apparition decrease in perihelion distance q (for example, from 1.30 au in 1996 to 1.21 au in 2021) has influenced the overall activity levels of 67P/C-G. Lara et al. (2011) and Bertaux et al. (2014) concluded that near-perihelion gas and/or dust production rates were not directly affected by the reduction in q . The 2021 water production rates from Keck and from Odin are within the range of Rosetta measurements in 2015 ($q = 1.24$ au), as reviewed in Section 3.3.

5. Conclusion

Because of the wealth of data, 67P/Churyumov–Gerasimenko is the best comet to date to discuss the similarities, differences, and uncertainties in results from various techniques applied to studies of volatiles. As measurements for both parent and product species are now available from the ground, such detailed comparison of retrieval methods is critical for full interpretation of coma abundances, and for better understanding the cosmogenic heritage preserved in the ice inventory of 67P/C-G. For this we advocate for a wide-scale collaboration across all measurement techniques from both in situ and remote sensing studies. One (but not exclusive) venue for such community effort could be the International Space Science Institute (Switzerland), which heavily promotes synergistic projects.

Acknowledgments

The authors wish to recognize and acknowledge the very significant cultural role and reverence that the summit of Maunakea has always had within the indigenous Hawaiian community. We are most fortunate and grateful to have the opportunity to conduct observations from this mountain.





The authors thank the anonymous referee for helpful comments.













The 2021 November 28 observations were allocated by NOIRLab (program R347), through the Telescope System Instrumentation Program (TSIP). TSIP was funded by NSF. The 2021 December 16 observations were carried out within the framework of Subaru-Keck/Subaru-Gemini time exchange program which is operated by the National Astronomical Observatory of Japan.

Various team members gratefully acknowledge NSF Astronomy and Astrophysics Research grants (AST-2009398, AST-2009910), the NASA Solar System Workings (80NSSC20K0651), Emerging Worlds (80NSSC20K0341), Solar System Observations (18-SSO18_2-0040; 80NSSC22K1401), and Rosetta Data Analysis (80NSSC18K1280) programs, Japan Society for the Promotion of Science KAKENHI Grants (JP20K14541 and JP21H04498), and the Planetary Science Division Internal Scientist Funding Program through the Fundamental Laboratory Research (FLaRe) work package.

This work benefited from discussions at the International Space Science Institute in Bern during meetings of International Team 361, “From Qualitative to Quantitative: Exploring the Early Solar System by Connecting Comet Composition and Protoplanetary Disk Models.”

ORCID iDs

Boncho P. Bonev  <https://orcid.org/0000-0002-6391-4817>
 Neil Dello Russo  <https://orcid.org/0000-0002-8379-7304>
 Hideyo Kawakita  <https://orcid.org/0000-0003-2011-9159>
 Ronald J. Vervack Jr.  <https://orcid.org/0000-0002-8227-9564>

Michael A. DiSanti  <https://orcid.org/0000-0001-8843-7511>
 Yoshiharu Shinnaka  <https://orcid.org/0000-0003-4490-9307>
 Takafumi Ootsubo  <https://orcid.org/0000-0002-5413-3680>
 Erika L. Gibb  <https://orcid.org/0000-0003-0142-5265>
 Michael R. Combi  <https://orcid.org/0000-0002-9805-0078>
 Kathrin Altwegg  <https://orcid.org/0000-0002-2677-8238>
 Nicolas Biver  <https://orcid.org/0000-0003-2414-5370>
 Geronimo L. Villanueva  <https://orcid.org/0000-0002-2662-5776>
 Younas Khan  <https://orcid.org/0000-0003-4773-2674>
 Mohammad Saki  <https://orcid.org/0000-0003-2277-6232>
 Adam J. McKay  <https://orcid.org/0000-0002-0622-2400>
 Anita L. Cochran  <https://orcid.org/0000-0003-4828-7787>
 Emmanuel Jehin  <https://orcid.org/0000-0001-8923-488X>
 Nathan X. Roth  <https://orcid.org/0000-0002-6006-9574>
 Martin A. Cordiner  <https://orcid.org/0000-0001-8233-2436>
 Yinsi Shou  <https://orcid.org/0000-0002-5765-9231>

References

- A’Hearn, M. F., Millis, R. C., Schleicher, D. O., Osip, D. J., & Birch, P. V. 1995, *Icar*, **118**, 223
- Altwegg, K. 2022, *PhT*, **75**, 34
- Altwegg, K., Balsiger, H., Berthelier, J.-J., et al. 2017, *RSPTA*, **375**, 20160253
- Bair, A., Schleicher, D., Knight, M., & Skiff, B. 2022, AAS DPS Meeting, **54**, 411.03
- Bauer, J. M., Fernández, Y. R., Protopapa, S., & Woodney, L. M. 2023, arXiv:2210.09400
- Bertaux, J.-L., Combi, M. R., Quémerais, E., & Schmidt, W. 2014, *P&SS*, **91**, 14
- Biver, N., Bockelée-Morvan, D., Hofstadter, M., et al. 2019, *A&A*, **630**, A19
- Biver, N., Bockelée-Morvan, D., Crovisier, J., et al. 2023b, *A&A*, **672**, A170
- Biver, N., Dello Russo, N., Opitom, C., & Rubin, M. 2023a, arXiv:2207.04800
- Bockelée-Morvan, D., Crovisier, J., Erard, S., et al. 2016, *MNRAS*, **462**, S170
- Bodewits, D., Bonev, B. P., Cordiner, M. A., & Villanueva, G. L. 2023, arXiv:2209.02616
- Bonev, B. P. 2005, PhD thesis, Univ. Toledo
- Bonev, B. P., Dello Russo, N., DiSanti, M. A., et al. 2021, *PSJ*, **2**, 45
- Bonev, B. P., DiSanti, M. A., Villanueva, G. L., et al. 2014, *ApJL*, **796**, L6
- Cheng, Y.-C., Bockelée-Morvan, D., Roos-Serote, M., et al. 2022, *A&A*, **663**, A43
- Cochran, A. L., Barker, E. S., & Gray, C. L. 2012, *Icar*, **218**, 144
- Cochran, A. L., Barker, E. S., Ramseyer, T. F., & Storrs, A. D. 1992, *Icar*, **98**, 151
- Combi, M., Shou, Y., Fougere, N., et al. 2020, *Icar*, **335**, 113421
- Cordiner, M. A., Roth, N. X., Milam, S. N., et al. 2023, *ApJ*, **953**, 59
- Crovisier, J., Colom, P., Gérard, E., Bockelée-Morvan, D., & Bourgois, G. 2002, *A&A*, **393**, 1053
- Dello Russo, N., DiSanti, M. A., Magee-Sauer, K., et al. 2004, *Icar*, **168**, 186
- Dello Russo, N., Kawakita, H., Vervack, R. J., & Weaver, H. A. 2016, *Icar*, **278**, 301
- DiSanti, M. A., Bonev, B. P., Gibb, E. L., et al. 2016, *ApJ*, **820**, 34
- DiSanti, M. A., Mumma, M. J., Dello Russo, N., & Magee-Sauer, K. 2001, *Icar*, **153**, 361
- Eistrup, C., Walsh, C., & van Dishoeck, E. F. 2019, *A&A*, **629**, A84
- Feaga, L., Sunshine, J., Bonev, B., et al. 2022, AAS DPS Meeting, **54**, 101.02
- Feldman, P. D., A’Hearn, M. F., & Festou, M. C. 2004, in *The New Rosetta Targets*, ed. L. Colangeli, E. M. Epifani, & P. Palumbo, Vol. 311 (Dordrecht: Kluwer), 47
- Fink, U. 2009, *Icar*, **201**, 311
- Fougere, N., Combi, M. R., Tenishev, V., et al. 2012, *Icar*, **221**, 174
- Gladman, B. 2005, *Sci*, **307**, 71
- Guilbert-Lepoutre, A., Schulz, R., Rozek, A., et al. 2014, *A&A*, **567**, L2
- Hänni, N., Altwegg, K., Combi, M., et al. 2022, *NatCo*, **13**, 3639
- Hansen, K. C., Altwegg, K., Berthelier, J.-J., et al. 2016, *MNRAS*, **462**, S491
- Ivanova, O. V., Rosenbush, V. K., Kiselev, N. N., Afanasiev, V. L., & Korsun, P. P. 2017, *MNRAS*, **469**, S386
- Kamp, I. 2020, IAU Proc. 345, Origins: From the Protosun to the First Steps of Life (Cambridge: Cambridge Univ. Press), 115
- Kelley, M. S. P., Sharma, K., Swain, V., et al. 2021, *ATel*, **15053**, 1
- Khan, Y., Gibb, E. L., Roth, N. X., et al. 2023, *AJ*, **165**, 231

- Knight, M. M., Kokotanekova, R., & Samarasinha, N. H. 2023, arXiv:2304.09309
- Knight, M. M., Snodgrass, C., Vincent, J.-B., et al. 2017, *MNRAS*, 469, S661
- Lara, L. M., Lin, Z. Y., Rodrigo, R., & Ip, W.-H. 2011, *A&A*, 525, A36
- Läuter, M., Kramer, T., Rubin, M., & Altwegg, K. 2020, *MNRAS*, 498, 3995
- Läuter, M., Kramer, T., Rubin, M., & Altwegg, K. 2022, *ACS Earth Space Chem.*, 6, 1189
- Le Roy, L., Altwegg, K., Balsiger, H., et al. 2015, *A&A*, 583, A1
- Levison, H. F. 1996, in ASP Conf. Ser. 107, Completing the Inventory of the Solar System, ed. T. W. Rettig & J. M. Hahn (San Francisco, CA: ASP), 173
- Martin, E. C., Fitzgerald, M. P., McLean, I. S., et al. 2018, *Proc. SPIE*, 10702, 107020A
- Müller, D. R., Altwegg, K., Berthelier, J.-J., et al. 2022, *A&A*, 662, A69
- Noonan, J. W., Parker, J., Harris, W. M., et al. 2023, *PSJ*, 4, 73
- Opitom, C., Snodgrass, C., Fitzsimmons, A., et al. 2017, *MNRAS*, 469, S222
- Rubin, M., Altwegg, K., Balsiger, H., et al. 2019, *MNRAS*, 489, 594
- Schleicher, D. G. 2006, *Icar*, 181, 442
- Schulz, R., Stüwe, J. A., & Boehnhardt, H. 2004, *A&A*, 422, L19
- Sharma, K., Kelley, M. S. P., Joharle, J., et al. 2021, *RNAAS*, 5, 277
- Shinnaka, Y., Fougere, N., Kawakita, H., et al. 2017, *AJ*, 153, 76
- Snodgrass, C., A'Hearn, M. F., Aceituno, F., et al. 2017, *RSPTA*, 375, 20160249
- Snodgrass, C., Feaga, L., Jones, G. H., Kueppers, M., & Tubiana, C. 2023, arXiv:2208.08476
- Snodgrass, C., Opitom, C., de Val-Borro, M., et al. 2016, *MNRAS*, 462, S138
- Vander Donckt, M., Aravind, K., Jehin, E., et al. 2023, in 14th Asteroids, Comets, and Meteors Conf. (Flagstaff, AZ: LPI), <https://www.hou.usra.edu/meetings/acm2023/pdf/2461.pdf>
- Villanueva, G. L., Liuzzi, G., Faggi, S., et al. 2022, Fundamentals of the Planetary Spectrum Generator (Greenbelt, MD: NASA)
- Villanueva, G. L., Mumma, M. J., Bonev, B. P., et al. 2009, *ApJL*, 690, L5
- Villanueva, G. L., Mumma, M. J., DiSanti, M. A., et al. 2011a, *Icar*, 216, 227
- Villanueva, G. L., Mumma, M. J., & Magee-Sauer, K. 2011b, *JGRE*, 116, E08012
- Villanueva, G. L., Smith, M. D., Protopapa, S., Faggi, S., & Mandell, A. M. 2018, *JQSRT*, 217, 86
- Willacy, K., Alexander, C., Ali-Dib, M., et al. 2015, *SSRv*, 197, 151
- Willacy, K., Turner, N., Bonev, B., et al. 2022, *ApJ*, 931, 164
- Xie, X., & Mumma, M. J. 1996, *ApJ*, 464, 457